 doi:10.20944/preprints202203.0050.v1

Article

Structure (epicardial stenosis) and function (microvascular dysfunction) that influences coronary fractional flow reserve estimation¶.

Jermiah J. Joseph[1,2], Clara Sun[1], Ting-Yim Lee[2,3], Daniel Goldman [2], Sanjay R. Kharche [1,2*], and Christopher W. McIntyre[1,2*]

[1] Lawson Health Research Institute, 750 Baseline Road East, London, ON N6C 2R5, Canada; jjosep56@uwo.ca (J.J.J); Clara.Sun@lhsc.on.ca (C.S.); Sanjay.Kharche@lhsc.on.ca (S.R.K.); Christopher.McIntyre@lhsc.on.ca (C.W.M.).

[2] Department of Medical Biophysics, Western University, 1151 Richmond Street North, London, ON N6A 5C1, Canada; jjosep56@uwo.ca (J.J.J); tlee@rri.ca (T-Y. L.); dgoldma2@uwo.ca (D.G.); Sanjay.Kharche@lhsc.on.ca (S.R.K.); Christopher.McIntyre@lhsc.on.ca (C.W.M.).

[3] Robarts Research Institute, Western University, 1151 Richmond Street North, London, ON N6A 5C1, Canada. tlee@rri.ca (T-Y. L.).

* Correspondence: Christopher.McIntyre@lhsc.on.ca (C.W.M.); Sanjay.Kharche@lhsc.on.ca (S.R.K.).

¶ This paper is an extended version of paper published in Functional Imaging and Modelling of the Heart 2021 in 11th International Conference, FIMH 2021, held in Stanford, CA, USA, 21–25 June 2021.

Abstract: *Background.* The treatment of coronary stenosis relies on invasive high risk surgical assessment to generate the fractional flow reserve diagnostics index, a ratio of distal to proximal pressures in respect of coronary atherosclerotic plaque causing stenosis. Non-invasive methods are therefore a need of the times. This study proposes an extensible mathematical description of the coronary vasculature that permits rapid estimation of the coronary fractional flow reserve. *Methods.* By adapting an existing closed loop model of human coronary blood flow, the effects of large vessel stenosis and microvascular disease on fractional flow reserve were quantified. Several simulations generated flow and pressure information which was used to compute fractional flow reserve under a spectrum of conditions including focal stenosis, diffuse stenosis, and microvascular disease. Sensitivity analysis stratified the influence of model parameters on the index. The model was simulated as coupled non-linear ordinary differential equations and numerically solved using an implicit higher order method. *Results.* Large vessel stenosis affected fractional flow reserve. The model predicts that the presence, rather than severity, of microvascular disease affect coronary flow deleteriously. Sensitivity analysis revealed that heart rate may not affect the index. *Conclusions.* The model provides a computationally inexpensive instrument for future *in silico* coronary blood flow investigations as well as clinical-imaging decision making. A combination of focal and diffuse stenosis appears to be essential in reducing the index. In addition to pressure measurements in the large epicardial vessels, diagnosis of microvascular disease is essential. The independence of the index with respect to heart rate suggests that computationally inexpensive steady state simulations may provide sufficient information to reliably compute the index.

Keywords: Coronary vasculature, lumped parameter model, fractional flow reserve, computational cardiology.

 doi:10.20944/preprints202203.0050.v1

1. Introduction.

This manuscript is an extension of work originally presented in Functional Imaging and Modelling of the Heart, 2021 [1].

Clinical relevance of and potential sources of uncertainty in fractional flow reserve estimation: Coronary vessel severity of the stenosis is clinically quantified using a quantity called fractional flow reserve (FFR) [2,3]. Quantities such as FFR allow objective clinical decision making especially when computed tomography subjectively indicates intermediate coronary stenosis. Several clinical trials have promoted the clinical acceptance of FFR for quantitative diagnostics [4-6]. FFR is clinically measured by determination of the ratio of blood flow through a stenosed vessel to that in a normal vessel [7]. The imaging burden on the patient is reduced by using pressure as a surrogate to blood flow, thereby eliminating the contrast enhanced imaging requirement of the hyperemic patient [7]. In recent times, non-invasive computed tomography angiography combined with computational fluid dynamics (CFD) has become increasing prevalent to estimate FFR, and aimed at reducing the significant risks associated with invasive pressure wire measurements [8]. However, multiple complex physiological processes render uncertainty to FFR estimation [9]. Particularly, the clinical literature suggests that micro-vascular dysfunction and stenosis morphology play a significant role in the estimated FFR. In addition, surgical and pharmacological sensitivity remains limited where adverse events often occur in critically ill patients such as those with renal failure [10] where diagnostics are sub-optimal.

A brief overview of coronary FFR modelling to date: The computed tomography angiography driven computational estimation of FFR is now an advanced technology [11]. Combining imaging with computational fluid dynamics assessment of FFR is known to increase the specificity of diagnosing lesion specific ischemia [12]. It is facilitated by ready availability of open source advanced scientific platforms [13-16] including those developed in house (Virtual Cardiac Physiology Laboratory) [17,18]. Typically, computation of FFR combines an imaging driven generation of 3D coronary anatomical geometry with a model of coronary physiology to provide boundary conditions including cardiac output, aortic pressure, and micro-vascular resistance, together in which appropriate laws of fluid flow physics simulate coronary hemodynamics. The approach has been deployed to study a spectrum of processes involving FFR estimation refinement [19], interplay among multiple stenosis complexes [20], and perioperative treatment assessment [21] among several other applications. Higher order 3D computational modelling is a high performance computing application and cannot be performed onsite by the clinician. Due to data heterogeneity resulting in the need to explore parameter spaces [22,23], large scale computations remain unwarranted in a clinical environment. Recent studies demonstrate the applicability of lumped parameter (0D) modelling. The role of peripheral arterial disease in hypertension was addressed using a human 0D model [24]. A detailed whole body human model tested the effects of treatments such as hypothermia and exercise on the systemic circulation [17]. The debilitating effects of atrial fibrillation on cerebral circulation were

illuminated by Hunter et al. [25]. However, computationally efficient modelling of coronary blood flow dynamics remains limited [26]. It is therefore relevant to make an open source and extensible lumped parameter model of the coronary circulation.

Study aims: In this work, an existing lumped parameter (0D) model of the coronary vasculature [27] was further developed and used to demonstrate important factors that regulate FFR. Specifically, the dependence of FFR on the nature of stenosis (focal or diffuse) and on micro-vascular status was investigated. Further, a PRCC based sensitivity analysis [1,28,29] was performed to stratify the impact of model parameters on FFR. For this purpose, a 0D modelling approach was found to be suitable as the study's goal was to understand coronary flow in the presence of pathological conditions. It can be appreciated that model identification (personalization), although highly desirable, was not essential in this theoretical study. As such, the presented model is theoretical in nature using which a better understanding of pathophysiological processes was prioritized over model personalization. The model has high manipulability and extensibility.

2. Methods.

Model development: A recent model of the coronary circulation [27] was adapted. It consists of 16 epicardial coronary artery segments including the left anterior descending (LAD), left circumflex artery (LCX), right coronary artery (RCA), and several of their clinically significant daughter segments. The closed loop conectivity of the structured tree network is illustrated in **Figure 1** and the names of all arteries are elaborated in **Table 1**. Each artery segment is chacterised by the Windkessel time independent parameters that consist of a hydraulic resistance (R_n), the intertia to flow of blood represented by an inductance (L_n), and the elastic capacity of the vessel, C_n [30]. The Windkessel parameters are determined using vessel lengths, vessel wall thickness, diameters, elasticity, blood viscosity, and blood density. In this study, blood viscosity was taken to be 4×10^{-3} kg/(m-s), density to be 10^3 kg/m^3, and elasticity (Young's modulus) to be 2×10^5 Pa. Vessel wall thickness, h, was estimated as h = 0.08 D [30]. Each artery segment entering a capillary bed leading into the venous circulation was further assumed to experience a microvasculature terminal impedance (Z_i) that was estimated using a structured tree model by Olufsen [31] as,

$$Z_i = \frac{8\mu\lambda((2\gamma^3)^{-(N+1)} - 1)}{\pi r_0^3 (0.5\gamma^{-3} - 1)}, \; i = 1, \ldots, 9. \quad \text{Equation 1.}$$

where $\gamma = 2^{-\frac{1}{\epsilon}}$ and ϵ represents the daughter vessel radius taper exponent, λ is the ratio of microvascular length to its diameter, and r_0 is the root vessel radius of the structured tree. N represents the number of generations for each structured tree [27,30,31]. The lumped coronary system was further developed by incorporating a detailed four chamber heart description (**Figure 1, A**) [32]. For simplicity, this model does not account for the phase altering effects of cardiac contractility on microvascular coronary flow.

Preprints (www.preprints.org) | NOT PEER-REVIEWED | Posted: 2 March 2022 doi:10.20944/preprints202203.0050.v1

Using the parameters given in **Tables 1 and 2,** and microvascular impedances calculated using Equation 1, pressure at each node of the model (**Figure 1)** was computed as

$$\frac{dP_n}{dt} = \frac{Q_n - Q_0}{C_n} \quad \text{Equation 2.}$$

and the flow through each vessel (resistance) was calculated as

$$\frac{dQ_n}{dt} = \frac{P_{n-1} - P_n - R_n Q_n}{L_n} \quad \text{Equation 3.}$$

Further, the flow through each of the terminal impedances was calculated as

$$Q_{z,n} = \frac{P_{n-1} - P_n}{Z_n} \quad \text{Equation 4.}$$

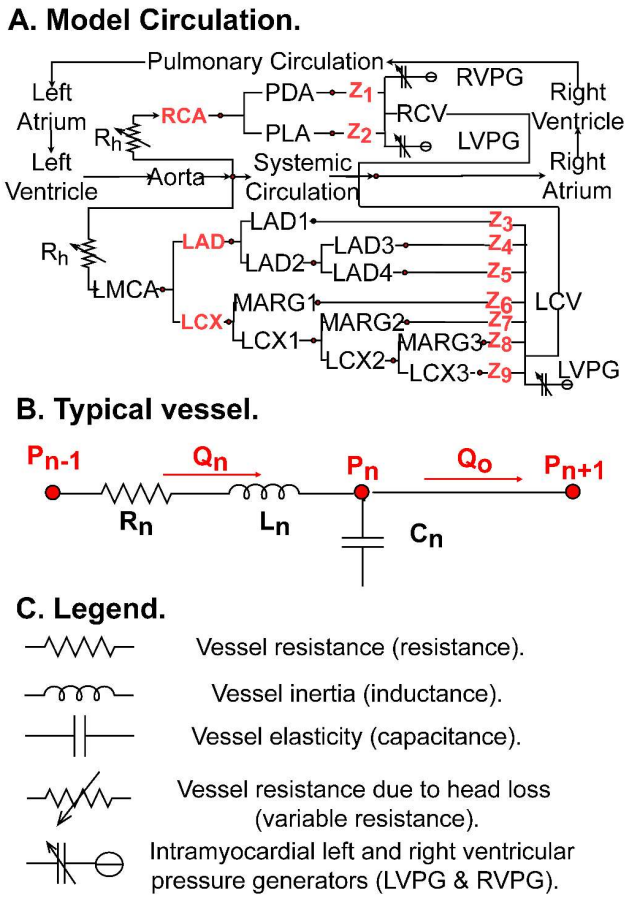

 doi:10.20944/preprints202203.0050.v1

Figure 1. The modelled lumped parameter coronary vasculature tree network. A. Closed loop vascular structure including tree network and functional components. See **Table 1** for vessel names. Z_i (i = 1 to 9) represent terminal vessel impedances. Vessels as well as impedances shown in red were used in the simulation experiments. B. Typical blood vessel represented by a resistance (R_n), inductance (L_n), and a capacitance (C_n). P_{n-1}: vessel inlet pressure; Q_n: flow through vessel; P_n: pressure in vessel; Q_o: outlet flow; P_{n+1}: outlet pressure, or pressure in distal vessel. C. Symbols used in panels A, B, and elsewhere in this work.

Simulation experiments: In all simulations, fractional flow reserve (FFR) was computed as the average of the ratio of the time dependent distal pressure, P_d (pressure downstream from stenosis) to the time dependent proximal (aortic) pressure, P_a,

$$FFR_{vessel} = \frac{1}{M}\sum_{n=1}^{n=M}\frac{P_{vessel,n}}{P_{aorta,n}} \quad \text{Equation 5.}$$

where M represents the total number of fractions over a given time T. Simulations were designed to explore the effects of stenosis severity in the largest epicardial vessels (either LAD, LCX, or RCA, see **Figure 1**) or microvascular disease, or both. A sensitivity analysis was performed as described below.

Stenosis in three large vessels, namely the left anterior descending artery (LAD), the left circumflex artery (LCX), and the right coronary artery (RCA), was investigated. Simulations were performed by imposing focal or diffuse stenosis in a given large vessel. To simulate focal stenosis, the blood vessel was divided into two and its biophysical parameters (**Table 1**) were revised using

$$\begin{aligned} R_s &= R_o\alpha^{-2} \\ C_s &= C_o\alpha^{3/2} \\ L_s &= L_o\alpha^{-1} \end{aligned} \quad \text{Equation 6}$$

where the stenosis severity, α, is given by the paramter

$$\alpha = \frac{A_s}{A_o}. \quad \text{Equation 7}$$

which is always between 0 and 1 by definition.

To simulate diffuse stenosis extended through a certain length percentage x_s ($0 \le x_s \le 1$) of a vessel, the revised parameters were calculated as

$$\begin{aligned} R &= R_s x_s + R_o(1-x_s) \\ L &= L_s x_s + L_o(1-x_s) \\ C &= C_s x_s + C_o(1-x_s) \end{aligned} \quad \text{Equation 8}$$

and used in Equations 2-4.

Microvascular disease was simulated by decreasing the terminal vessel radius by a predefined amount in all terminals. In this model, radius regulated microvascular impedance was increased by decreasing the ϵ in Equation 1's γ parameter.

 doi:10.20944/preprints202203.0050.v1

Sensitivity analysis: Sensitivity of multiple model paramters including stenosis lengths, focal stenosis severity, heart rate, terminal vessel impedences, microvascular veseel taper paramter (ε), and number of downstream vasculature generatetions to FFR was computed. To do so, we used our implementation of partial ranked cor-relation coefficients (PRCC) [17,33]. The coefficients were used to rank the parameters in descending order of significance, and the most relevant results reported.

Numerical methods: The model is a system of 36 coupled stiff ordinary differential equations. Pressures and flows were computed as state variables according to governing ordinary differntial equations, Equations 2 to 4 for each vessel. The system was solved using our robust implicit solver available in our simulation software [18,24]. The method used in the solver is based on implicit backward difference formulae that provides $O(dt^6)$ accuracy. A maximum user time step of 0.005 s gave stable solutions which remained unaffected when the maximum time step was halved and doubled. Each instance generated 500 s of simulated dynamics from which the final 10 s of activity were used to generate results. Simulations were performed on local and national clusters. Each instance of the model is a serial run that took 15 seconds. To construct results in the presented work, a large number of model instances (10^6) for predefined values of physiologically relevant parameters were executed within 4 hours using 48 processors. The trivially parallel simulations were performed using GNU Utilities [34]. The simulation outputs were post-processed using a combination of UNIX and MATLAB scripts.

Table 1. Model parameter values. See **Figure 1** for vessel connectivity. The rows are colour coded to suggest the major epicardial coronaries, either LAD, LCX, or RCA.

Vessel	R (mmHg-s/ml)	C (ml/mmHg x 10^{-3})	L (mmHg-s^2/ml)
LMCA	0.2299	2.9	0.00228
LAD	0.4662	1.6	0.0298
LAD1	0.5729	1.6	0.0342
LAD2	1.7077	3.4	0.0916
LAD3	3.7484	1.3	0.1115
LAD4	3.2930	0.4	0.0716
LCX	0.3929	1.2	0.0241
LCX1	0.4730	0.7	0.0231
LCX2	1.0264	0.7	0.0380
LCX3	3.2342	1.1	0.0944
MARG1	1.7351	1.2	0.0655
MARG2	2.9195	0.8	0.0787
MARG3	3.0683	1	0.0896
RCA	1.8302	6.3	0.1171
PLA	2.4412	1.1	0.0799

 doi:10.20944/preprints202203.0050.v1

PDA	1.2571	1.8	0.0596

Table 2. Parameters used to compute microvascular impedances.

Z (Figure 1).	Root vessel radius, r_0 (mm).		N.	Control Z values (mmHg-s/ml).
Z_1	PDA	0.108	19	134.100
Z_2	PLA	0.130	20	083.710
Z_3	LAD1	0.146	20	059.095
Z_4	LAD3	0.103	19	154.592
Z_5	LAD4	0.088	18	227.185
Z_6	MARG1	0.116	19	108.224
Z_7	MARG2	0.098	19	179.482
Z_8	MARG3	0.102	19	159.184
Z_9	LCX3	0.102	19	159.184

Legend. Z: terminal impedance; N: number of generations in microvasculature.

3. Results

Model FFR during the cardiac cycle: Time dependent FFR in the three major coronary arteries (LAD, LCX, and RCA) under predefined large vessel stenosis and microvascular disease is illustrated in **Figure 2**. The control simulation (**Figure 2**, **top row**) devoid of stenosis or microvascular disease shows that FFR is high (more than 0.8) during the complete cardiac cycle in all three vessels. Due to flow distribution from the aorta to the smaller coronary network, the time dependent FFR was seen to reduce during systole. The time dependent FFR when either LAD, LCX, or RCA were focally stenosed by 90% ($\alpha = 0.9$) is shown in **Figure 2**, **middle row**. When there was a full vessel length stenosis the FFR values reduced to 0.56 for the LAD, 0.52 for the LCX, and 0.5 for the RCA. Whereas the overall FFR was observed to reduce significantly in all three simulations, large vessel stenosis led to minimal FFR during the cardiac cycle's diastole. Simulated microvascular disease, simulated by augmenting all terminal impedances by 50% ($\varepsilon = 2.55$, a reduction of ε increases impedance, Z), led to amplifying the difference between the aortic and respective distal pressures and gave a minimal FFR estimate during the systole (**Figure 2**, **bottom row**). When microvascular disease was simulated the maximum time dependent FFR value was calculated to be 1 and minimum to be 0.7 in all three blood vessels.

Preprints (www.preprints.org) | NOT PEER-REVIEWED | Posted: 2 March 2022 doi:10.20944/preprints202203.0050.v1

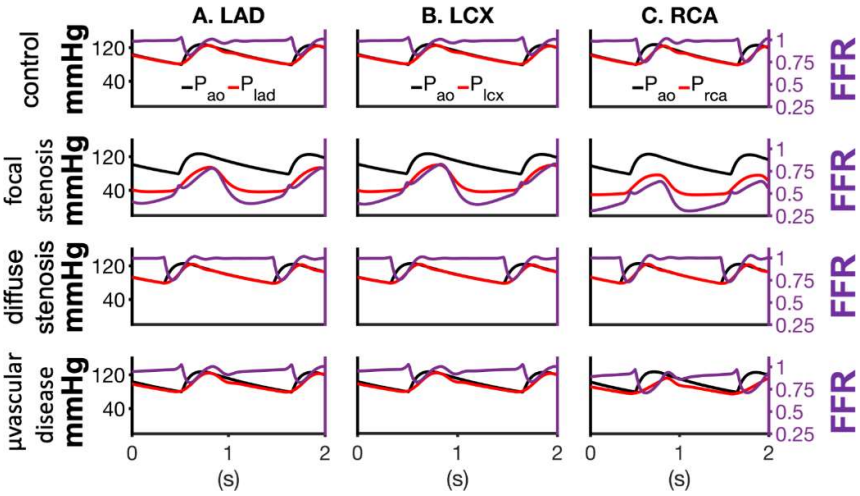

Figure 2. Pressure profiles and FFR in the LAD (column A), LCX (column B), and RCA (column C). In all columns, top row shows non stenosed model behavior, second row shows the result of focal stenosis ($\boldsymbol{\alpha} = \mathbf{90\%}$), and third row shows the result of downstream microvascular disease in the absence of focal stenosis ($\boldsymbol{\alpha} = \mathbf{100\%}$; $\boldsymbol{\epsilon} = \mathbf{2.33}$). In all panels, black lines and axis represent aortic pressure (proximal pressure) while red lines and axis represent the pressure of vessel of interest (distal pressure). Time dependent FFR is shown as orange dashed lines.

The coronary flow in the control coronary model (**Figure 3**, **top row**) and its reduction due to focal stenosis (**Figure 3**, **middle row**), and microvascular disease (**Figure 3, bottom row)** was computed**.** Relative to the control case (**Figure 3, top row)**, focal stenosis (**Figure 3, second row**) restricted flow significantly in all 3 blood vessels. When microvascular disease was implemented, the maximum flow and overall flow in the network decreased. Further, the impact of individual artery resistances, inertances, and compliances were blunted as reflected in the flow profiles (**Figure 3**, **bottom row**).

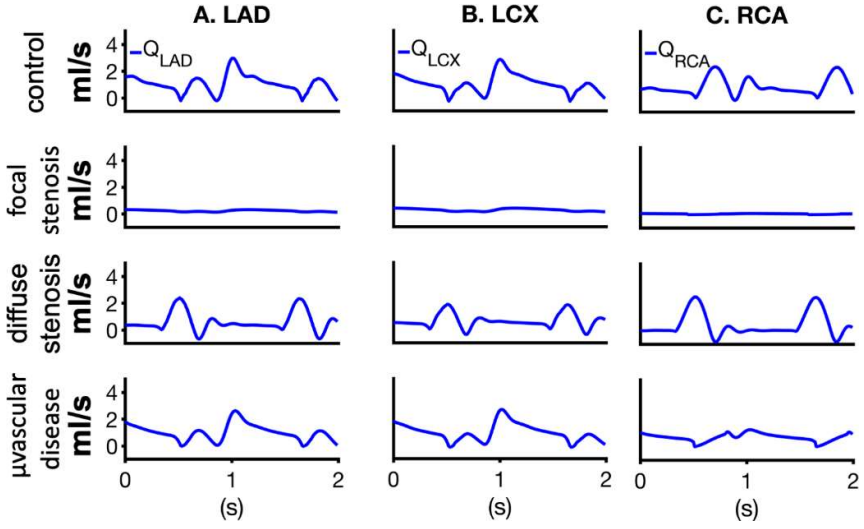

Figure 3. Flow profiles in the LAD (column A), LCX (column B), and RCA (column C). In all columns, top row shows non-stenosed (control) model flow, second row shows flow under focal stenosis ($\boldsymbol{\alpha}$ **= 90%**) and the third row shows the flow under microvascular disease in the absence of focal stenosis ($\boldsymbol{\alpha}$ **= 100%;** $\boldsymbol{\epsilon}$ **= 2.33**).

Preprints (www.preprints.org) | NOT PEER-REVIEWED | Posted: 2 March 2022 doi:10.20944/preprints202203.0050.v1

Focal and diffuse stenosis interplay: The dependence of average flow (flow), maximum flow, and FFR on simultaneous presence of reduced vessel diameters (focal stenosis) and diffuse stenosis (reduction of diameters along a predefined length) were quantified (**Figure 4)**. In all vessels, the detrimental effects of stenosis on flow (**Figure 4, top row**) and maximum flow (**Figure 4, middle row)** were impacted by the severity of focal stenosis (horizontal axis) to a greater extent than the severity of diffuse stenosis (vertical axis). Progressive focal stenosis alone was found to minimally impact the estimated FFR (**Figure 4**, bottom row) due to the model formulation (see above). As such, a reduction of FFR was observed when the stenosis was diffuse to a certain extent. Conversely, diffuse stenosis in the absence of focal stenosis (vertical axis in **Figure 4**) also did not reduce FFR. Progressive focal stenosis in the RCA caused the largest reduction of FFR (**Figure 4, third row**) as compared to focal stenosis in the LAD and LCX in the presented model. In the presented model, the RCA was more susceptible to FFR reduction due to stenosis in comparison to the LAD and LCX. Simultaneous presence of focal and diffuse stenosis caused the most severe reduction of FFR in the RCA, followed by in the LAD and LCX.

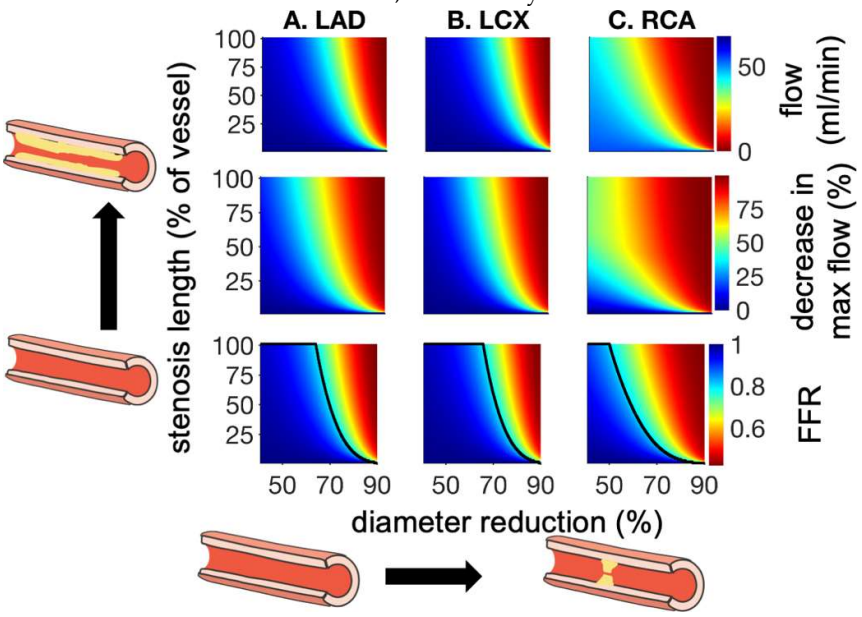

Figure 4. Dependence of flow rate (top row), maximum flow (middle row), and mean FFR (bottom row) on stenosis length (vertical axis, all panels) and vessel diameter (horizontal axis, all panels). Columns A, B, and C show LAD, LCX, and RCA results respectively. The black line in the bottom row demarcates the FFR = 0.8 threshold.

Role of microvascular disease in the modelled FFR: The average flow (flow), maximum flow, and FFR values of simultaneous focal stenosis and microvascular disease are shown in **Figure 5.** Microvascular disease was simulated by varying the daughter vessel's radius taper exponent ϵ (**Equation 1**) from 2.76 (0% microvascular disease, control) to 2.33 (100% microvascular disease) which represents turbulent flow [22]. At diameter reductions below 70%, the flow in each blood vessel (**Figure 5, top row**) is significantly restricted by up to half of the control flow with the increase in severity of microvascular disease. At similar diameter reductions in the LAD and LCX however, the peak reduction in max flow values (near 0.5 of the control values) occur at 50% microvascular disease and

 doi:10.20944/preprints202203.0050.v1

returns to near control values at maximal microvascular disease At diameter reductions above 80% , microvascular exacerbates the effect of the stenosis on FFR values. However, an almost unique value of diameter reduction for each, LAD, LCX, and RCA, was observed to characterize a clinically significant FFR transition to below 0.8 in the presence of an arbitrary severity microvascular disease. While the diameter reduction was 0.7 for LAD and LCX, it was seen to be a much lower 0.55 in case of the RCA.

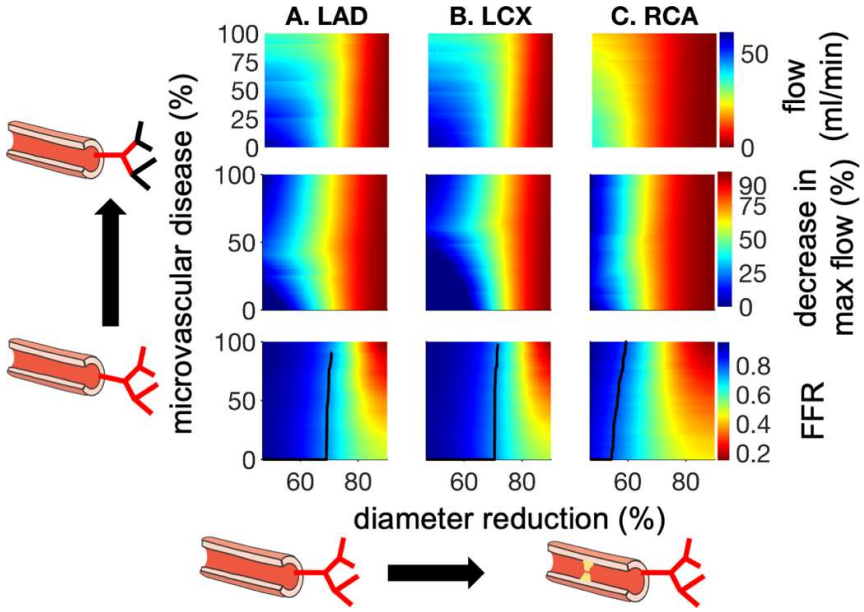

Figure 5. Dependence of flow rate (top row), maximum flow (middle row), and mean FFR (bottom row) on microvascular resistance increase (microvascular disease, vertical axis in all panels) and vessel diameter (horizontal axis, all panels). Columns A, B, and C show LAD, LCX, and RCA results respectively. The black line in the bottom row demarcates the FFR = 0.8 threshold.

Sensitivity analysis to stratify FFR impacting parameters: The results of the sensitivity analysis are shown in **Figures 6 and 7**. The histograms of FFR values obtained during the PRCC calculation are shown in **Figure 6**. As can be seen, the model did not produce any instances with FFR less than 0.3 due to the ranges of parameters considered. The model appears to produce FFR values centered around 0.54. Further, in all 3 coronaries the FFR values appear to be distributed in a left skewed Gaussian manner.

Preprints (www.preprints.org) | NOT PEER-REVIEWED | Posted: 2 March 2022 doi:10.20944/preprints202203.0050.v1

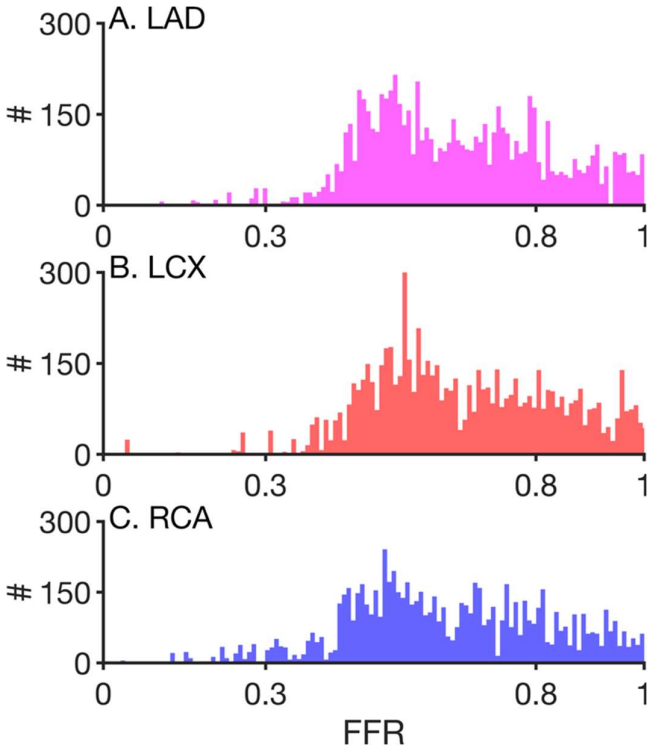

Figure 6. Histograms of FFR obtained from PRCC simulations (see **Figure 7**). Panel A shows the data for LAD, panel B for LCX, and panel C for RCA.

The sensitivity analysis generated PRCC coefficients are shown in **Figure 7**. The heart rate (HR) is the most impactful model parameter regulating the FFR. Consistently, focal stenosis (fs) is also a significant regulator of PRCC. Both HR and fs negatively regulate FFR. Diffuse stenosis (ds) and the right ventricular systolic elastance ($E_{sys,rv}$) also negatively regulate FFR. The microvascular parameters (microvascular root radius r_0, and tapering factor ε) also affect FFR according to our sensitivity analysis.

 doi:10.20944/preprints202203.0050.v1

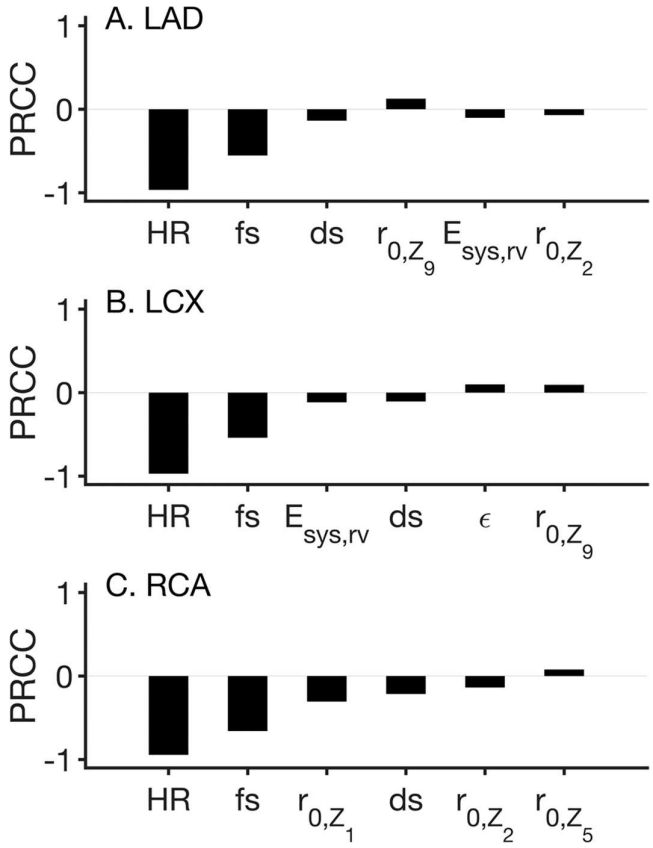

Figure 7. PRCC sensitivity of FFR to model control parameters. In all panels, the sensitivity of FFR to the six most relevant parameters are shown. Panel A shows the PRCC for LAD, panel B for the LCX, and panel C for the RCA. In all panels, HR: heart rate; fs: focal stenosis; ds: diffuse stenosis; r_0: root radius of microvascular bed; Z_i: microvascular impedance; ε: microvasculature taper exponent; and $E_{sys,rv}$: systolic elastance of the right ventricle.

4. Limitations and Future Directions.

Further development of the presented model will lead to its clinical applicability. Whereas a detailed heart model [35] was incorporated into the lumped parameter description [27], the simulated aortic root inflow to the coronary vasculature remains generic. Upon availability, patient specific aortic root blood flow profiles will alleviate the limitation. In a similar manner, the vessel parameters and microvascular impedances were summarized from the literature [27,30]. Patient specific model identification will increase the applicability of the model and reduce its prediction uncertainty. The inclusion of vessel specific biomechanical properties and inclusion of a reactive vascular tone module [36-38] is expected to allow simulation of clinical parameters such as pulse wave velocities and residence times [39-44]. The inclusion of autoregulatory processes will further assist to make the model's FFR estimates quantitatively reliable [45].

Although the model is theoretical in nature, the presented results will guide our future work. As such, the findings of the study remain informative for deeper lumper parameter modelling and will inform our spatially extended modelling.

4. Conclusions and Discussion.

 doi:10.20944/preprints202203.0050.v1

Focal and diffuse coronary stenosis were both observed to modulate FFR (**Figure 3**). However, our simulations indicate that FFR estimation must consider other conditions such as AF and microvascular disease, both of which are routinely diagnosed among patients using non-invasive techniques. Furthermore, it appears that blood flow to the right ventricle is more severely affected due to the extra-coronary and RCA stenosis conditions (**Figures 4, 5**). Novel imaging protocols that account for cardiac chamber to chamber diastole will fortify further refinement of the diagnostic instrument.

As seen in **Figure 4**, focal as well as diffuse stenosis reduces FFR relative to the control case. However, it can also be seen that extra-coronary conditions such as microvascular disease also affect FFR estimates. It is therefore clear that consideration of the effects of co-morbidities is essential in FFR estimation. The result also indicates that our approach is suitable for ranking the severity of co-morbidities. Specially, **Figure 3**, indicates that microvascular disease alone does affect FFR estimation (see definition of FFR). Furthermore, the left and right heart's coronary are affected differentially. Whereas imaging studies are optimized to provide information regarding left coronaries, the model suggests that the right coronaries should also be considered. Our model suggests that stenosis may not be an exclusive focal or diffuse phenomenon. As **Figure 4** shows, consideration of a combination of the two natures of stenosis is essential, especially in our future higher dimensional modelling (see **Figure 8**). In future studies, the 0D models in this detailed investigation will be useful as boundary conditions to 3D model computational fluid dynamics [46]. In addition to detailed geometry, **Figure 5** indicates that *a priori* knowledge of microvascular health status will permit 3D models to provide better FFR estimates. Within the confines of the presented model, the sensitivity analysis (**Figure 7**) suggests that heart rate and severity of the large vessel occlusion are prime regulators of FFR. In addition, systolic heart function was found to be relevant.

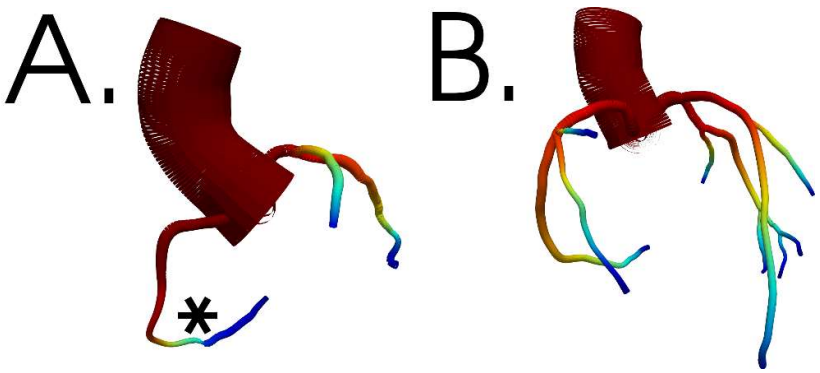

Figure 8. Pressure (arbirtrary units) distribution in two representative solid models generated using our recent imaging data (unpublished). The '*' in panel A indicates the stenosis location.

A lumped parameter model of the human coronary vasculature [27] was further developed in this study. The model is capable of personalization based on clinical measurements of aortic pressure waves, imaging based vascular geometry (lengths, radii, and morphometry), as well as cardiac wall motion kinematics [47]. As such, the model permits

imaging-clinical data assessment as a computationally efficient instrument, prior to detailed 3D computational fluid dynamics simulations. This theoretical study illuminated the relative relevance of focal and diffuse stenosis. It also suggests that knowledge of co-morbidities will improve our clinical diagnostics. Furthermore, it pre-informed our upcoming 3D investigation regarding the clinical data that will permit both validation as well as prediction.

Author Contributions: Study design: J.J.J., S.R.K., C. W. M.; model development, J.J.J.; simulations: J.J.J. and C. S.; data analysis and figures, J.J.J.; draft writing, J.J.J. and S. R. K.; final manuscript, S.R.K., J.J.J., C. S., T. L., D.G. and C.W.M.; funding secured by S.R.K., D.G., and C. W. M. All authors have read and agreed to the final version of the manuscript.

Funding: This research was funded by Canada Canarie Inc. [RS3-111], Canadian NSERC grant [R4081A03] and Canada Heart and Stroke Foundation [G-20-0028717].

Institutional Review Board Statement: This study did not use sensitive data, patient information, or any other identity data. This computational study did not require ethics approvals of any nature.

Informed Consent Statement: This computational study did not require consent from patients or otherwise.

Data Availability Statement: The authors agree to make the model data openly available upon the publication of the manuscript. The model code is available in our laboratory's GITHUB at: https://github.com/mccsssk2/MDPI2022_JermiahsCoronary

Acknowledgments: This work was supported by Canada Canarie Inc. (project: RS3-111), partly by Canadian Heart and Stroke Foundation grant (G-20-0028717, PI: CWM), and partly by Canadian NSERC grant (R4081A03, PI: Daniel Goldman). This work is part of CS's research based undergraduate training in Western University. SRK also thanks Lawson Health Research Institute, Western University, MITACS Globalink (Canada), and Compute Canada for funding, compute, labor, and other resources. We thank the FIMH 2021 organizers for the opportunity to disseminate our work. We thank Ms. Shambhavi Malik (IIT BHU, shambhavimalik.bme18@itbhu.ac.in) for assistance with the spatially extended modelling of **Figure 8**.

Conflicts of Interest: The authors declare no conflict of interest.

References

1. Joseph, J.J.; Lee, T.-Y.; Goldman, D.; McIntyre, C.W.; Kharche, S.R. The Role of Extra-Coronary Vascular Conditions that Affect Coronary Fractional Flow Reserve Estimation. 2021; pp. 595-604.
2. Pijls, N.H.; Fearon, W.F.; Tonino, P.A.; Siebert, U.; Ikeno, F.; Bornschein, B.; van't Veer, M.; Klauss, V.; Manoharan, G.; Engstrom, T.; et al. Fractional flow reserve versus angiography for guiding percutaneous coronary intervention in patients with multivessel coronary artery disease: 2-year follow-up of the FAME (Fractional Flow Reserve Versus Angiography for Multivessel Evaluation) study. *J Am Coll Cardiol* **2010**, *56*, 177-184, doi:10.1016/j.jacc.2010.04.012.
3. Pijls, N.H.; Van Gelder, B.; Van der Voort, P.; Peels, K.; Bracke, F.A.; Bonnier, H.J.; el Gamal, M.I. Fractional flow reserve. A useful index to evaluate the influence of an epicardial coronary stenosis on myocardial blood flow. *Circulation* **1995**, *92*, 3183-3193.

4. Fearon, W.F.; Tonino, P.A.; De Bruyne, B.; Siebert, U.; Pijls, N.H. Rationale and design of the Fractional Flow Reserve versus Angiography for Multivessel Evaluation (FAME) study. *Am Heart J* **2007**, *154*, 632-636, doi:10.1016/j.ahj.2007.06.012.
5. Fearon, W.F.; Bornschein, B.; Tonino, P.A.; Gothe, R.M.; Bruyne, B.D.; Pijls, N.H.; Siebert, U.; Fractional Flow Reserve Versus Angiography for Multivessel Evaluation Study, I. Economic evaluation of fractional flow reserve-guided percutaneous coronary intervention in patients with multivessel disease. *Circulation* **2010**, *122*, 2545-2550, doi:10.1161/CIRCULATIONAHA.109.925396.
6. Pijls, N.H.; van Schaardenburgh, P.; Manoharan, G.; Boersma, E.; Bech, J.W.; van't Veer, M.; Bar, F.; Hoorntje, J.; Koolen, J.; Wijns, W.; et al. Percutaneous coronary intervention of functionally nonsignificant stenosis: 5-year follow-up of the DEFER Study. *J Am Coll Cardiol* **2007**, *49*, 2105-2111, doi:10.1016/j.jacc.2007.01.087.
7. Tonino, P.A.; De Bruyne, B.; Pijls, N.H.; Siebert, U.; Ikeno, F.; van' t Veer, M.; Klauss, V.; Manoharan, G.; Engstrom, T.; Oldroyd, K.G.; et al. Fractional flow reserve versus angiography for guiding percutaneous coronary intervention. *N Engl J Med* **2009**, *360*, 213-224, doi:10.1056/NEJMoa0807611.
8. Ball, C.; Pontone, G.; Rabbat, M. Fractional Flow Reserve Derived from Coronary Computed Tomography Angiography Datasets: The Next Frontier in Noninvasive Assessment of Coronary Artery Disease. *BioMed research international* **2018**, *2018*, 2680430, doi:10.1155/2018/2680430.
9. Jeremias, A.; Stone, G.W. Fractional flow reserve for the evaluation of coronary stenoses: limitations and alternatives. *Catheterization and cardiovascular interventions : official journal of the Society for Cardiac Angiography & Interventions* **2015**, *85*, 602-603, doi:10.1002/ccd.25851.
10. Odudu, A.; Francis, S.T.; McIntyre, C.W. MRI for the assessment of organ perfusion in patients with chronic kidney disease. *Current opinion in nephrology and hypertension* **2012**, *21*, 647-654, doi:10.1097/MNH.0b013e328358d582.
11. Taylor, C.A.; Fonte, T.A.; Min, J.K. Computational fluid dynamics applied to cardiac computed tomography for noninvasive quantification of fractional flow reserve: scientific basis. *J Am Coll Cardiol* **2013**, *61*, 2233-2241, doi:10.1016/j.jacc.2012.11.083.
12. Coenen, A.; Lubbers, M.M.; Kurata, A.; Kono, A.; Dedic, A.; Chelu, R.G.; Dijkshoorn, M.L.; Gijsen, F.J.; Ouhlous, M.; van Geuns, R.J.; et al. Fractional flow reserve computed from noninvasive CT angiography data: diagnostic performance of an on-site clinician-operated computational fluid dynamics algorithm. *Radiology* **2015**, *274*, 674-683, doi:10.1148/radiol.14140992.
13. Updegrove, A.; Wilson, N.M.; Merkow, J.; Lan, H.; Marsden, A.L.; Shadden, S.C. SimVascular: An Open Source Pipeline for Cardiovascular Simulation. *Ann Biomed Eng* **2017**, *45*, 525-541, doi:10.1007/s10439-016-1762-8.
14. Arthurs, C.J.; Khlebnikov, R.; Melville, A.; Marcan, M.; Gomez, A.; Dillon-Murphy, D.; Cuomo, F.; Silva Vieira, M.; Schollenberger, J.; Lynch, S.R.; et al. CRIMSON: An open-source software framework for cardiovascular integrated modelling and simulation. *PLoS Comput Biol* **2021**, *17*, e1008881, doi:10.1371/journal.pcbi.1008881.
15. McCullough, J.W.S.; Richardson, R.A.; Patronis, A.; Halver, R.; Marshall, R.; Ruefenacht, M.; Wylie, B.J.N.; Odaker, T.; Wiedemann, M.; Lloyd, B.; et al. Towards blood flow in the virtual human: efficient self-coupling of HemeLB. *Interface focus* **2021**, *11*, 20190119, doi:10.1098/rsfs.2019.0119.
16. Randles, A.; Draeger, E.W.; Bailey, P.E. Massively parallel simulations of hemodynamics in the primary large arteries of the human vasculature. *J Comput Sci* **2015**, *9*, 70-75, doi:10.1016/j.jocs.2015.04.003.
17. Joseph, J.J.; Hunter, T.J.; Sun, C.; Goldman, D.; Kharche, S.R.; McIntyre, C.W. Using a Human Circulation Mathematical Model to Simulate the Effects of Hemodialysis and Therapeutic Hypothermia. *Applied Sciences* **2022**, *12*, 307.

18. Kharche, S.R.; Lemoine, S.; Tamasi, T.; Hur, L.; So, A.; McIntyre, C.W. Therapeutic Hypothermia Reduces Peritoneal Dialysis Induced Myocardial Blood Flow Heterogeneity and Arrhythmia. *Front Med (Lausanne)* **2021**, *8*, 700824, doi:10.3389/fmed.2021.700824.
19. Ghorbanniahassankiadeh, A.; Marks, D.S.; LaDisa, J.F. Correlation of Computational Instantaneous Wave-Free Ratio With Fractional Flow Reserve for Intermediate Multivessel Coronary Disease. *Journal of biomechanical engineering* **2021**, *143*, doi:10.1115/1.4049746.
20. Vardhan, M.; Gounley, J.; Chen, S.J.; Chi, E.C.; Kahn, A.M.; Leopold, J.A.; Randles, A. Non-invasive characterization of complex coronary lesions. *Scientific reports* **2021**, *11*, 8145, doi:10.1038/s41598-021-86360-6.
21. Chandola, G.; Zhang, J.M.; Tan, R.S.; Chai, P.; Teo, L.; Allen, J.C.; Low, R.; Huang, W.; Leng, S.; Fam, J.M.; et al. Computed Tomography Coronary Angiography and Computational Fluid Dynamics Based Fractional Flow Reserve Before and After Percutaneous Coronary Intervention. *Frontiers in bioengineering and biotechnology* **2021**, *9*, 739667, doi:10.3389/fbioe.2021.739667.
22. Jonasova, A.; Vimmr, J. On the relevance of boundary conditions and viscosity models in blood flow simulations in patient-specific aorto-coronary bypass models. *International journal for numerical methods in biomedical engineering* **2021**, *37*, e3439, doi:10.1002/cnm.3439.
23. Vignon-Clementel, I.E.; Figueroa, C.A.; Jansen, K.E.; Taylor, C.A. Outflow boundary conditions for 3D simulations of non-periodic blood flow and pressure fields in deformable arteries. *Computer methods in biomechanics and biomedical engineering* **2010**, *13*, 625-640, doi:10.1080/10255840903413565.
24. Altamirano-Diaz, L.; Kassay, A.D.; Serajelahi, B.; McIntyre, C.W.; Filler, G.; Kharche, S.R. Arterial Hypertension and Unusual Ascending Aortic Dilatation in a Neonate With Acute Kidney Injury: Mechanistic Computer Modeling. *Frontiers in Physiology* **2019**, *10*, doi:10.3389/fphys.2019.01391.
25. Hunter, T.J.; Joseph, J.J.; Anazodo, U.; Kharche, S.R.; McIntyre, C.W.; Goldman, D. Atrial Fibrillation and Anterior Cerebral Artery Absence Reduce Cerebral Perfusion: A De Novo Hemodynamic Model. *Applied Sciences* **2022**, *12*, 1750.
26. Olufsen, M.S.; Nadim, A. On deriving lumped models for blood flow and pressure in the systemic arteries. *Mathematical biosciences and engineering : MBE* **2004**, *1*, 61-80, doi:10.3934/mbe.2004.1.61.
27. Duanmu, Z.; Yin, M.; Fan, X.; Yang, X.; Luo, X. A patient-specific lumped-parameter model of coronary circulation. *Scientific reports* **2018**, *8*, 874, doi:10.1038/s41598-018-19164-w.
28. Kharche, S.R.; Mironova, G.Y.; Goldman, D.; McIntyre, C.W.; Welsh, D.G. Sensitivity Analysis of a Smooth Muscle Cell Electrophysiological Model. Cham, 2021; pp. 540-550.
29. Britton, O.J.; Bueno-Orovio, A.; Van Ammel, K.; Lu, H.R.; Towart, R.; Gallacher, D.J.; Rodriguez, B. Experimentally calibrated population of models predicts and explains intersubject variability in cardiac cellular electrophysiology. *Proc Natl Acad Sci U S A* **2013**, *110*, E2098-2105, doi:10.1073/pnas.1304382110.
30. Pietrabissa, R.; Mantero, S.; Marotta, T.; Menicanti, L. A lumped parameter model to evaluate the fluid dynamics of different coronary bypasses. *Medical engineering & physics* **1996**, *18*, 477-484, doi:10.1016/1350-4533(96)00002-1.
31. Olufsen, M.S. Structured tree outflow condition for blood flow in larger systemic arteries. *Am J Physiol-Heart C* **1999**, *276*, H257-H268, doi:10.1152/ajpheart.1999.276.1.H257.
32. Heldt, T.; Shim, E.B.; Kamm, R.D.; Mark, R.G. Computational modeling of cardiovascular response to orthostatic stress. *J Appl Physiol (1985)* **2002**, *92*, 1239-1254, doi:10.1152/japplphysiol.00241.2001.
33. Marino, S.; Hogue, I.B.; Ray, C.J.; Kirschner, D.E. A methodology for performing global uncertainty and sensitivity analysis in systems biology. *J Theor Biol* **2008**, *254*, 178-196, doi:10.1016/j.jtbi.2008.04.011.

34. Tange, O. GNU Parallel - The Command-Line Power Tool. *The USENIX Magazine* **2011**, 42-47.
35. Heldt, T. Continuous blood pressure-derived cardiac output monitoring--should we be thinking long term? *J Appl Physiol (1985)* **2006**, *101*, 373-374, doi:10.1152/japplphysiol.00502.2006.
36. Arciero, J.C.; Carlson, B.E.; Secomb, T.W. Theoretical model of metabolic blood flow regulation: roles of ATP release by red blood cells and conducted responses. *Am J Physiol Heart Circ Physiol* **2008**, *295*, H1562-1571, doi:10.1152/ajpheart.00261.2008.
37. Lucker, A.; Secomb, T.W.; Barrett, M.J.P.; Weber, B.; Jenny, P. The Relation Between Capillary Transit Times and Hemoglobin Saturation Heterogeneity. Part 2: Capillary Networks. *Front Physiol* **2018**, *9*, 1296, doi:10.3389/fphys.2018.01296.
38. Pries, A.R.; Secomb, T.W. Microcirculatory network structures and models. *Ann Biomed Eng* **2000**, *28*, 916-921, doi:10.1114/1.1308495.
39. Clavica, F.; Alastruey, J.; Borlotti, A.; Sherwin, S.J.; Khir, A.W. One-dimensional computational model of pulse wave propagation in the human bronchial tree. *Conf Proc IEEE Eng Med Biol Soc* **2010**, *2010*, 2473-2476, doi:10.1109/IEMBS.2010.5626559.
40. Poleszczuk, J.; Debowska, M.; Dabrowski, W.; Wojcik-Zaluska, A.; Zaluska, W.; Waniewski, J. Patient-specific pulse wave propagation model identifies cardiovascular risk characteristics in hemodialysis patients. *PLoS Comput Biol* **2018**, *14*, e1006417, doi:10.1371/journal.pcbi.1006417.
41. Womersley, J.R. Oscillatory flow in arteries. II. The reflection of the pulse wave at junctions and rigid inserts in the arterial system. *Phys Med Biol* **1958**, *2*, 313-323.
42. Butty, V.D.; Gudjonsson, K.; Buchel, P.; Makhijani, V.B.; Ventikos, Y.; Poulikakos, D. Residence times and basins of attraction for a realistic right internal carotid artery with two aneurysms. *Biorheology* **2002**, *39*, 387-393.
43. Esmaily-Moghadam, M.; Hsia, T.Y.; Marsden, A.L. A non-discrete method for computation of residence time in fluid mechanics simulations. *Phys Fluids (1994)* **2013**, *25*, 110802, doi:10.1063/1.4819142.
44. Hashemi, J.; Patel, B.; Chatzizisis, Y.S.; Kassab, G.S. Study of Coronary Atherosclerosis Using Blood Residence Time. *Frontiers in Physiology* **2021**, *12*, doi:10.3389/fphys.2021.625420.
45. Carlson, B.E.; Arciero, J.C.; Secomb, T.W. Theoretical model of blood flow autoregulation: roles of myogenic, shear-dependent, and metabolic responses. *Am J Physiol Heart Circ Physiol* **2008**, *295*, H1572-1579, doi:10.1152/ajpheart.00262.2008.
46. Marsden, A.; Moghadam, M.E. Multiscale Modeling of Cardiovascular Flows for Clinical Decision Support. *Applied Mechanics Reviews* **2015**, *67*.
47. Crowley, L.E.; McIntyre, C.W. Remote ischaemic conditioning[mdash]therapeutic opportunities in renal medicine. *Nature reviews. Nephrology* **2013**, *9*, 739-746, doi:10.1038/nrneph.2013.226.